Naval Research Laboratory

Washington, DC 20375-5320

NRL/MR/6410--11-9339

Computational Fluid Dynamics Study for a Deep Stall Air Vehicle

RAVI RAMAMURTI

Center for Reactive Flow and Dynamical Systems
Laboratory for Computational Physics and Fluid Dynamics

May 31, 2011

Approved for public release; distribution is unlimited.

REPORT DOCUMENTATION PAGE

Form Approved
OMB No. 0704-0188

Public reporting burden for this collection of information is estimated to average 1 hour per response, including the time for reviewing instructions, searching existing data sources, gathering and maintaining the data needed, and completing and reviewing this collection of information. Send comments regarding this burden estimate or any other aspect of this collection of information, including suggestions for reducing this burden to Department of Defense, Washington Headquarters Services, Directorate for Information Operations and Reports (0704-0188), 1215 Jefferson Davis Highway, Suite 1204, Arlington, VA 22202-4302. Respondents should be aware that notwithstanding any other provision of law, no person shall be subject to any penalty for failing to comply with a collection of information if it does not display a currently valid OMB control number. **PLEASE DO NOT RETURN YOUR FORM TO THE ABOVE ADDRESS.**

1. REPORT DATE *(DD-MM-YYYY)*	**2. REPORT TYPE**	**3. DATES COVERED** *(From - To)*
31-05-2011	Memorandum Report	

4. TITLE AND SUBTITLE

Computational Fluid Dynamics Study for a Deep Stall Air Vehicle

5a. CONTRACT NUMBER

5b. GRANT NUMBER

5c. PROGRAM ELEMENT NUMBER
EW114-002-6073

6. AUTHOR(S)

Ravi Ramamurti

5d. PROJECT NUMBER

5e. TASK NUMBER

5f. WORK UNIT NUMBER
64-6073-A-0

7. PERFORMING ORGANIZATION NAME(S) AND ADDRESS(ES)

Naval Research Laboratory
4555 Overlook Avenue, SW
Washington, DC 20375-5320

8. PERFORMING ORGANIZATION REPORT NUMBER

NRL/MR/6410--11-9339

9. SPONSORING / MONITORING AGENCY NAME(S) AND ADDRESS(ES)

10. SPONSOR / MONITOR'S ACRONYM(S)

11. SPONSOR / MONITOR'S REPORT NUMBER(S)

12. DISTRIBUTION / AVAILABILITY STATEMENT

Approved for public release; distribution is unlimited.

13. SUPPLEMENTARY NOTES

14. ABSTRACT

The aerodynamic characteristics of a vehicle in deep-stall conditions are investigated and the motion of the vehicle is predicted in a self-consistent manner. Three-dimensional unsteady computations of the complete aircraft with prescribed control surface deflections are carried out. Both steady and unsteady flow simulations are performed to map out the lift, drag, and moment as a function of various flight and control surface parameters. The unsteady forces and moments were computed, and the resulting unconstrained trajectory based on the 6-dof model of the vehicle is simulated at high angles of attack.

15. SUBJECT TERMS
Deep-stall
Aerodynamics
Incompressible flow
Unstructured grid

16. SECURITY CLASSIFICATION OF:			**17. LIMITATION OF ABSTRACT**	**18. NUMBER OF PAGES**	**19a. NAME OF RESPONSIBLE PERSON**
a. REPORT	**b. ABSTRACT**	**c. THIS PAGE**			Ravi Ramamurti
Unclassified	Unclassified	Unclassified	UL	20	**19b. TELEPHONE NUMBER** *(include area code)* (202) 767-0608

Standard Form 298 (Rev. 8-98)
Prescribed by ANSI Std. Z39.18

Table of Contents

INTRODUCTION **1**

THE INCOMPRESSIBLE FLOW SOLVER **1**

THE COMPUTATIONAL MODEL **2**

RESULTS AND DISCUSSION **3**

Effect of angle of attack: *4*
Effect of Side Slip angle: *5*
Effect of Rudder deflection: *6*
Effect of Aileron deflection: *7*
Effect of the Elevator: *9*
Deep-Stall Flow: *9*

SUMMARY **16**

ACKNOWLEDGEMENTS **16**

REFERENCES **16**

List of Figures

Fig. 1. Digitization of the vehicle geometry: a) drawing of the wing tip and b) digitized points. ..2
Fig. 2. CAD representation of the Deep-Stall Vehicle. 2
Fig. 3. Computational Coordinate system for Deep-Stall Vehicle. 3
Fig. 4. Lift, drag and pitch moment characteristics of the Deep-Stall Vehicle. 4
Fig. 5. Lift, drag and side force coefficients, vehicle trim angle = 0°. 5
Fig. 6. Moment Coefficients, vehicle trim angle = 0°. 5
Fig. 7. Lift, drag and side force coefficients, vehicle trim angle = 3°. 5
Fig. 8. Moment Coefficients, vehicle trim angle = 3°. 6
Fig. 9. Lift, drag and side force coefficients, vehicle trim angle = 0°. 6
Fig. 10. Moment Coefficients, vehicle trim angle = 0°. 6
Fig. 11. Lift, drag and side force coefficients, vehicle trim angle = 3°. 7
Fig. 12. Moment Coefficients, vehicle trim angle = 3°. 7
Fig. 13. Lift, drag and side force coefficients, vehicle trim angle = 0°. 7
Fig. 14. Moment Coefficients, vehicle trim angle = 0°. 8
Fig. 15. Lift, drag and side force coefficients, vehicle trim angle = 3°. 8
Fig. 16. Moment Coefficients, vehicle trim angle = 3°. 8
Fig. 17. Lift, drag and pitch moment coefficients, vehicle trim angle = 0° 9
Fig. 18. Lift, drag and pitch moment coefficients, vehicle trim angle = 3° 9
Fig. 19. Unsteady forces for a deep stall configuration, V = 1.67 m/s. 10
Fig. 20. Surface pressure distribution on a Deep Stall vehicle, V = 1.67 m/s, α = 70° 10
Fig. 21. Mean forces and moments for Deep-Stall vehicle, V = 5.79 m/s, β = 0°. 11
Fig. 22. Mean forces and moments for Deep-Stall vehicle, V = 5.79 m/s, α = 70°. 11
Fig. 23. Variation of Mean forces and moments for Deep-Stall vehicle with left aileron deflection, V = 5.79 m/s, α = 70°. 12

Fig. 24. Time history of forces and moments on a deep-stall vehicle, V = 10.97 m/s, α = 40°....12
Fig. 25. Trajectory of the deep-stall vehicle, V = 10.97 m/s, α = 40°.....13
Fig. 26. Surface pressure distribution on the vehicle undergoing deep-stall maneuver, t = 2.38 s. 13
Fig. 27. Time history of forces and moments on a deep-stall vehicle with differential aileron deflection $\Delta\theta$ = 15°, V = 10.97 m/s, α = 40°. 14
Fig. 28. Trajectory of a deep-stall vehicle with differential aileron deflection $\Delta\theta$ = 15°, V = 10.97 m/s, α = 40°. 14
Fig. 29. Time history of forces and moments on a deep-stall vehicle with differential aileron deflection $\Delta\theta$ = 30°, V = 10.97 m/s, α = 40°. 15
Fig. 30. Trajectory of a deep-stall vehicle with differential aileron deflection $\Delta\theta$ = 30°, V = 10.97 m/s, α = 40°. 15

Computational Fluid Dynamics Study for a Deep Stall Air Vehicle

INTRODUCTION

Unmanned air vehicles (UAVs) have become an integral part of the battle-space environment. Small camera-equipped vehicles have shown their value in recent conflicts. These vehicles can be assembled and launched from small spaces, but recovery of these vehicles still poses difficulties. Recovery of these aircraft typically requires a long open space for landing. In order to minimize the space required for recovery it is desired to design a vehicle capable of flight at high angles of attack. High angle-of-attack flight could also provide greater obstacle avoidance capabilities when flying in urban terrain since the turning radius in high angle-of-attack flight is greatly reduced as compared to that of conventional forward flight. Sensing capabilities could also be enhanced through the use of sensor pointing without the complexity and weight of morphing aircraft or gimbaled sensors.

Small UAVs have received recent attention for several urban missions due to their rapidly maturing flight capabilities. These small man-portable vehicles feature a deep-stall mode in which the elevator is deflected and the power is reduced. The aircracft then descends steeply in a near level attitude until it touches the ground. An example of such a vehicle is the Raven, developed by Aerovironment [1], which utilizes the wing geometry to remain stable in deep-stall. At high angles of attack, the flight of these vehicles are often characterized by wing rock. A possible cause for this phenomenon is the unsteady shedding of vortices from the wing and further interaction of this flow with the airframe downstream.

In order to operate these small UAVs in deep-stall, Aaron Kahn of the U.S. Naval Research Laboratory has developed an adaptive controller [2] capable of regulating vehicle attitude in the presence of large model errors. The focus of the current study is to obtain the aerodynamic characteristics of the vehicle in the deep stall regime. An unstructured grid-based unsteady Navier-Stokes solver with automatic adaptive remeshing capability, called FEFLO, was used to compute the flow about the deep-stall vehicle.

THE INCOMPRESSIBLE FLOW SOLVER

The governing equations employed are the incompressible Navier-Stokes equations in Arbitrary Lagrangian-Eulerian (ALE) formulation which are written as

$$\frac{d\mathbf{v}}{dt} + \mathbf{v}_a \cdot \nabla \mathbf{v} + \nabla p = \nabla \cdot \sigma, \tag{1}$$

$$\nabla \cdot \mathbf{v} = 0, \tag{2}$$

where p denotes the pressure, $\mathbf{v}_a = \mathbf{v} - \mathbf{w}$ the advective velocity vector, where $\mathbf{v}$ is the flow velocity and $\mathbf{w}$ is the mesh velocity w and the material derivative is with respect to the mesh velocity $\mathbf{w}$. Both the pressure p and the stress tensor σ have been normalized by the (constant) density ρ and are discretized in time using an implicit time stepping procedure. Thus the equations are Eulerian for zero mesh velocity and Lagrangian if the mesh velocity is the same as the flow velocity. The present time-accurate flow solver is discretized in space using a Galerkin procedure with linear tetrahedral elements. The details of the flow solver have already been

Manuscript approved February 18, 2011.

discussed extensively elsewhere, Ramamurti *et. al.* [3-6], in connection with successfully validated solutions for numerous 2-D and 3-D, laminar and turbulent, steady and unsteady flow problems.

THE COMPUTATIONAL MODEL

The initial critical and time consuming step for flow simulations is the generation of a 3-D surface model that is suitable for computational fluid dynamics. This is achieved by converting the longitudinal cross-sectional drawing of the vehicle to a digitized format using ImageJ [7]. For example, Fig. 1 shows the drawing of the wing tip and the digitized points. These digitized sections are then assembled using FECAD, the CAD software used in conjunction with the FEFLO software suite. The CAD representation of the complete deep-stall vehicle is shown in Fig. 2.

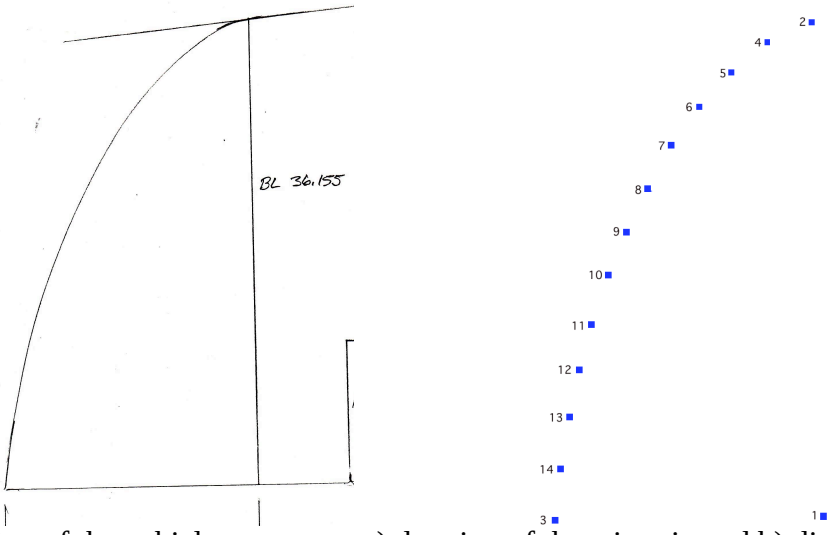

Fig. 1. Digitization of the vehicle geometry: a) drawing of the wing tip and b) digitized points.

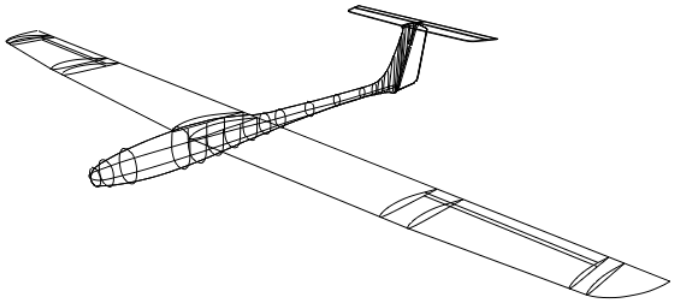

Fig. 2. CAD representation of the Deep-Stall Vehicle.

RESULTS AND DISCUSSION

In order to determine the steady state aerodynamic characteristics of this vehicle, a tetrahedral mesh consisting of 1.2 M points and 6.8 M tetrahedral elements. The geometry used to evaluate the pitch characteristics employed a symmetry plane and therefore only half the geometry shown in Fig. 2 is used. For determining side-slip characteristics and computing unsteady flow past the vehicle, a domain consisting of approximately, 2.8 M points and 16.0 M tetrahedral elements is employed. The forces and moments were obtained by integrating the surface pressure over the various segments of the vehicle, such as the wing and the fuselage, in the fixed coordinate system (XYZ), shown in Fig. 3. The resulting forces were transformed to the vehicle coordinate system (xyz) using the rotation transformation, Eq. 1. In this coordinate system, the *x*-axis is aligned with the flow velocity vector, and α and β are the angle of attack and side-slip, respectively. In order to keep the transformation general, the roll angle ϕ is also included.

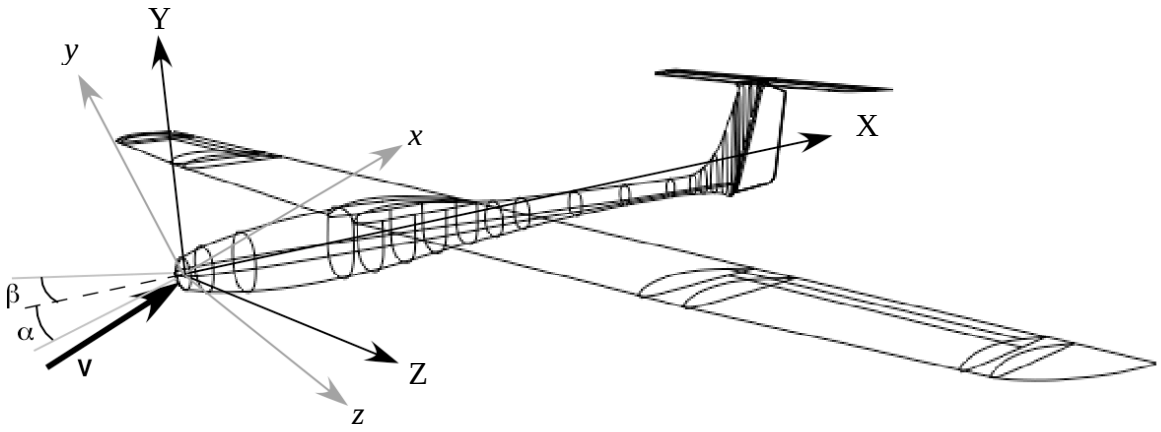

Fig. 3. Computational Coordinate system for Deep-Stall Vehicle.

$$\begin{Bmatrix} x \\ y \\ z \end{Bmatrix} = \begin{bmatrix} \cos\alpha\cos\beta & \sin\alpha\cos\beta & -\sin\beta \\ \cos\alpha\sin\beta\sin\phi - \sin\alpha\cos\phi & \sin\alpha\sin\beta\sin\phi + \cos\alpha\cos\phi & \cos\beta\sin\phi \\ \cos\alpha\sin\beta\cos\phi + \sin\alpha\sin\phi & \sin\alpha\sin\beta\cos\phi - \cos\alpha\sin\phi & \cos\beta\cos\phi \end{bmatrix} \begin{Bmatrix} X \\ Y \\ Z \end{Bmatrix} \tag{1}$$

The computed forces (F_X, F_Y ,F_Z) are transformed to their respective drag, lift and side forces (*D, L, N*) which are normalized using the free stream velocity *V*, the density of air ρ, and the area of the wing A_w.

$$C_D = \frac{D}{\frac{1}{2}\rho V^2 A_w}, \quad C_L = \frac{L}{\frac{1}{2}\rho V^2 A_w} \text{ and } C_N = \frac{N}{\frac{1}{2}\rho V^2 A_w} \tag{2 a-c}$$

The moments are further normalized by the average wingspan, $S = A_w/C$, where C = 0.171m is the chord length of the wing.

Effect of angle of attack:

The steady flow characteristics are obtained for a vehicle speed, V = 13.41 m/s, and for various angles of attack and side-slip. Figure 4 shows the lift, drag and pitch moment variation as the angle of attack is increased. The forces and moments on just the wing surfaces and the complete vehicle are shown. It can be seen that for α's in the range of (-10°, 15°), the lift variation is nearly linear, as expected. The vehicle stalls for α > 15° shown by the drop in lift and shows a modest increase in lift beyond 25°. At α = 0°, the drag force on the vehicle is approximately 0.29 N, yielding C_{D0} of 4.614×10^{-3}; the corresponding lift is 8.48 N and C_L is 0.2392. At α = 15°, the lift and drag forces are 58.878 N and 5.2 N, respectively. The Reynolds number for this flow based on the chord length is approximately 153,000. Hence, a viscous flow past this configuration was simulated at both 0° and 15° angles of attack. The resulting forces show that at α = 0°, the lift and drag forces are 8.29N and 0.62N, respectively; at α = 15°, the lift and drag forces are 57.97 N and 5.55 N, respectively.

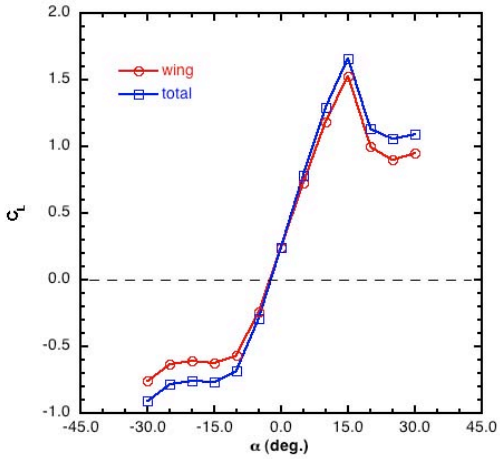

a. Lift coefficient

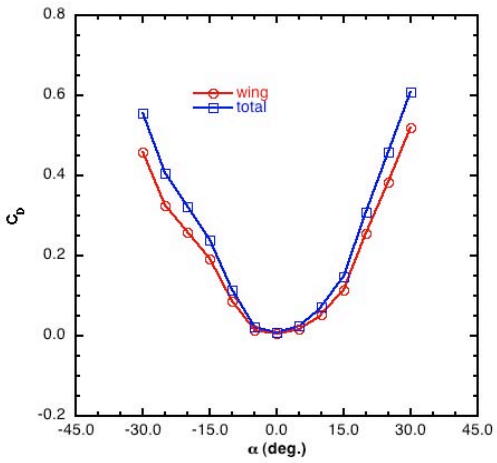

b. Drag Coefficient

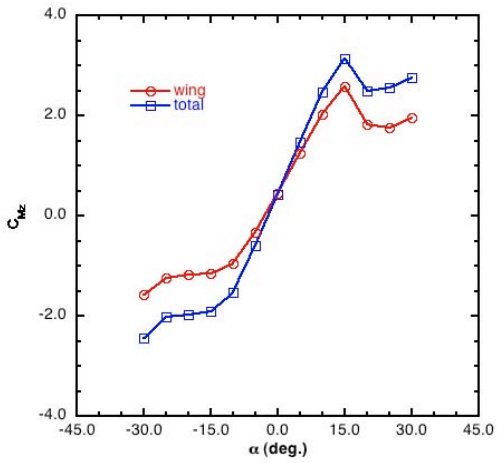

c. Pitch moment Coefficient

Fig. 4. Lift, drag and pitch moment characteristics of the Deep-Stall Vehicle.

Effect of Side Slip angle:

In order to assess the characteristics of the vehicle with respect to the side slip angle, the flow past the vehicle was simulated over a range ±15°, with the vehicle trimmed at two different angles, 0° and 3°. Figures 5-8 show the variation of lift, drag and side forces and the moment coefficients. These results show that the side force coefficient, C_N, and the moment coefficients about the *x* and *y*-axes are linear with respect to the side-slip angle, as expected. The lift, drag and roll moment coefficients show a parabolic variation. As the trim angle is increased form 0° to 3°, the C_L increases by 0.3, Figs. 5a and 7a, and the C_D also increases, while the C_N remains nearly unchanged, as shown in Figs. 5c and 7c.

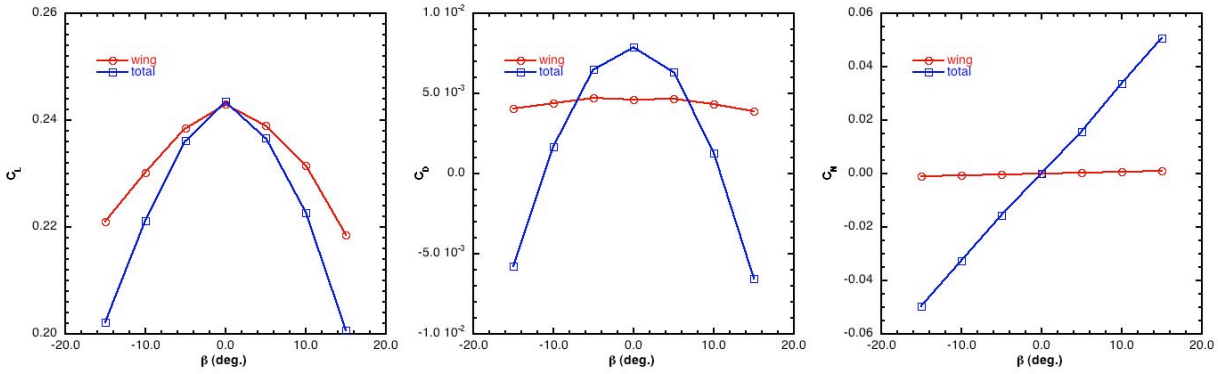

a. Lift b. Drag c. Side force

Fig. 5. Lift, drag and side force coefficients, vehicle trim angle = 0°.

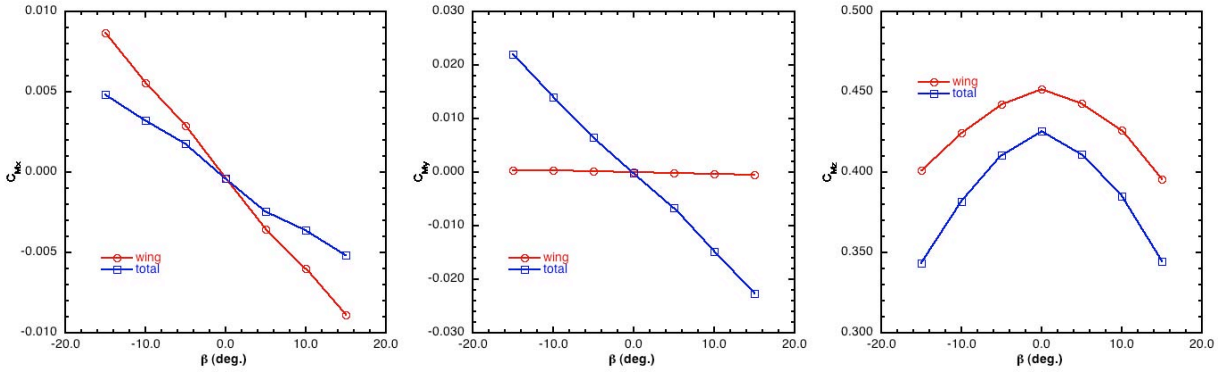

a. C_{Mx} b. C_{My} c. C_{Mz}

Fig. 6. Moment Coefficients, vehicle trim angle = 0°.

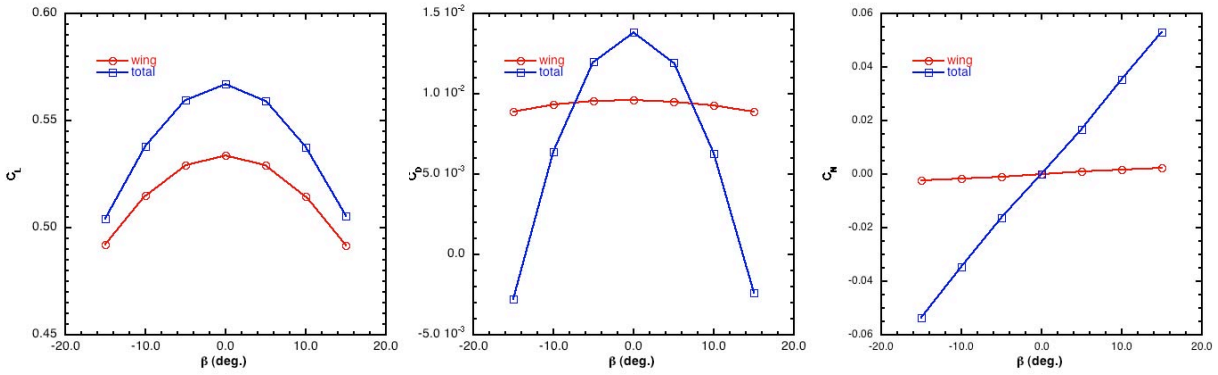

a. Lift b. Drag c. Side force

Fig. 7. Lift, drag and side force coefficients, vehicle trim angle = 3°.

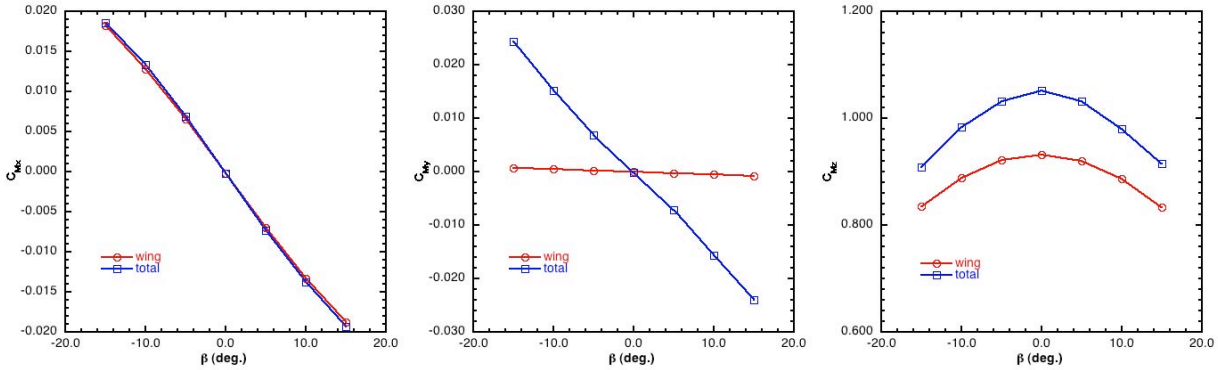

a. C_{Mx} b. C_{My} c. C_{Mz}

Fig. 8. Moment Coefficients, vehicle trim angle = 3°.

Effect of Rudder deflection:

The effect of the rudder deflection on the forces and moments were computed for two deflections of ±5°, and for three side slip angles of 0° and ±15°. Figures 9a and b show that C_L variation with respect to the rudder deflection remains same while the C_D for rudder deflection $\delta = 5°$ and $\beta = -15°$ is the same as that of $\delta = -5°$ and $\beta = 15°$, as expected. The side force coefficient is increased by nearly 0.023, as shown in Fig. 9c. The change in the yaw moment, C_{My}, due to the rudder deflection of 10° is nearly 0.012, and the change in the roll moment, C_{Mx},

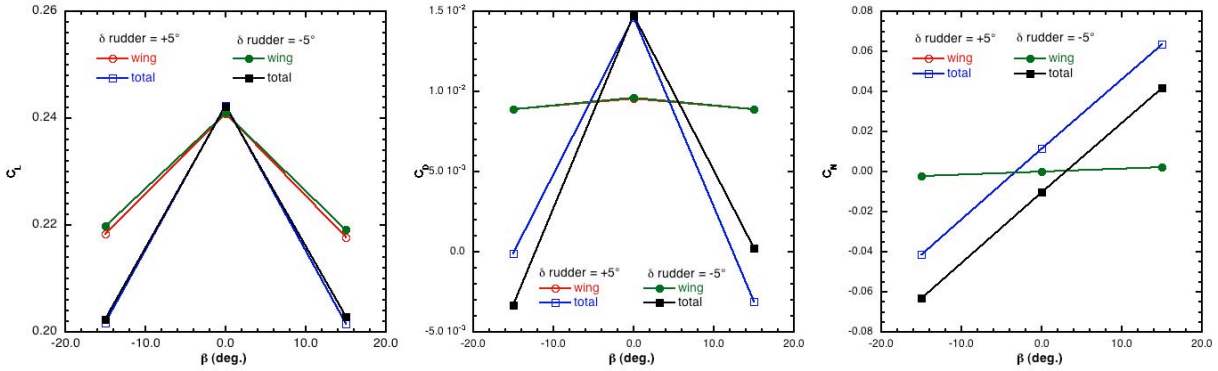

a. Lift b. Drag c. Side force

Fig. 9. Lift, drag and side force coefficients, vehicle trim angle = 0°.

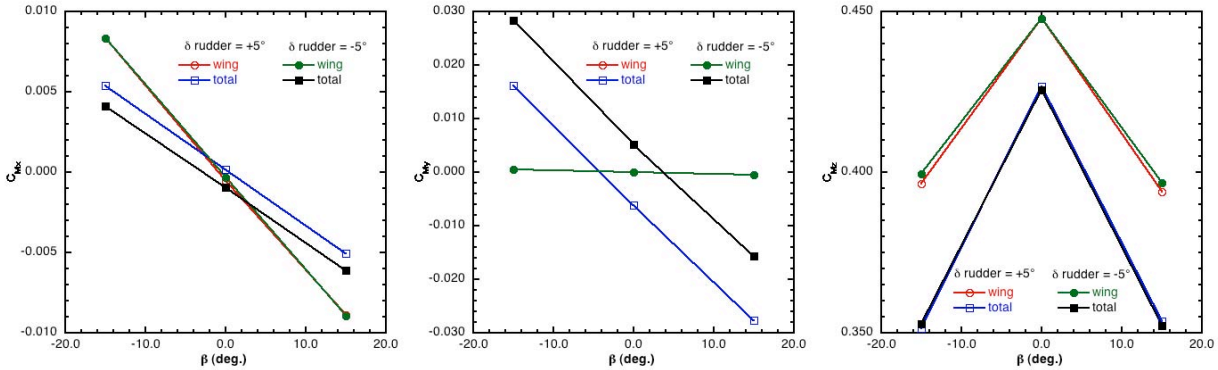

a. C_{Mx} b. C_{My} c. C_{Mz}

Fig. 10. Moment Coefficients, vehicle trim angle = 0°.

is 0.001, as shown in Figs. 10a and b. The pitch moment remains unchanged due to the rudder deflection, as expected. Similar results are obtained for the 3° trim case, in Figs. 11 and 12.

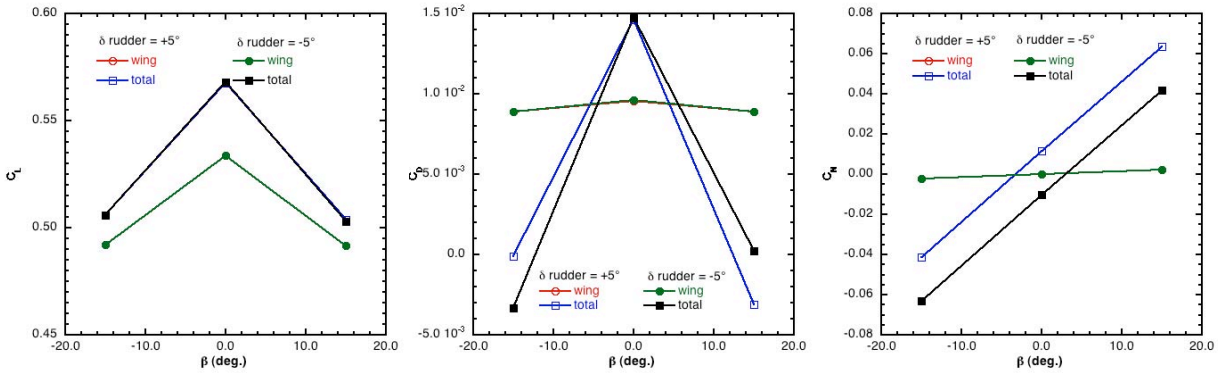

a. Lift b. Drag c. Side force

Fig. 11. Lift, drag and side force coefficients, vehicle trim angle = 3°.

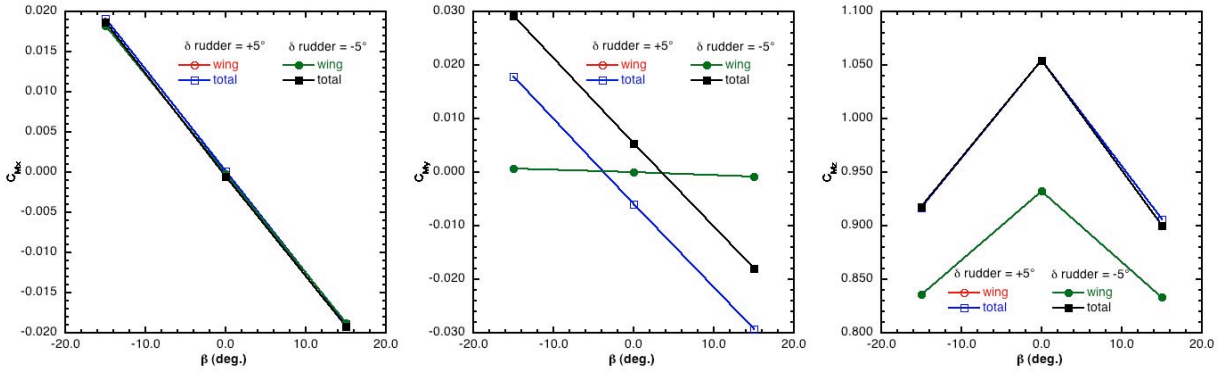

a. C_{Mx} b. C_{My} c. C_{Mz}

Fig. 12. Moment Coefficients, vehicle trim angle = 3°.

Effect of Aileron deflection:

In order or study the effect of the aileron deflection on the roll characteristics of the vehicle, the left aileron is deflected in a counterclockwise (+ve θ) direction about the Z-axis (Fig.2), and the right aileron is deflected in a clockwise direction by the same angle. Simulations are performed for four aileron deflections and for side-slip angles of 0° and 15°. Figure 13a shows

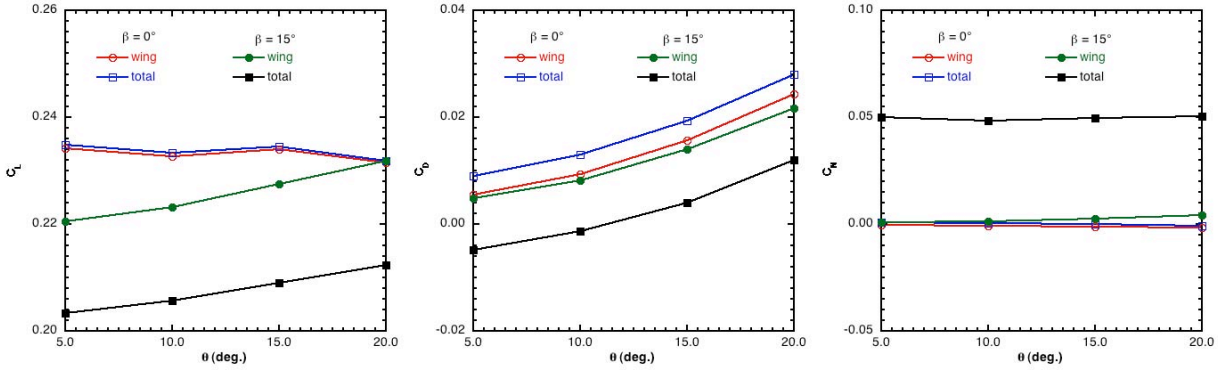

a. Lift b. Drag c. Side force

Fig. 13. Lift, drag and side force coefficients, vehicle trim angle = 0°.

that the lift remains nearly unchanged for β = 0° and a loss of lift for β = 15°. The drag force increases as the aileron deflection is increased, Fig. 13b, and the side force remains constant for non-zero side-slip angle, Fig. 13c. The effect of the aileron deflection on the moments is shown in Fig. 14. The roll moment and the pitch moment for non-zero side slip varies linearly with the aileron deflection, shown in Figs. 14a and c, while the yaw moment and the pitch moment at zero side slip are nearly constant, shown in Figs. 14b and c. Similar results are obtained for the vehicle trimmed at 3°, Figs. 15 and 16.

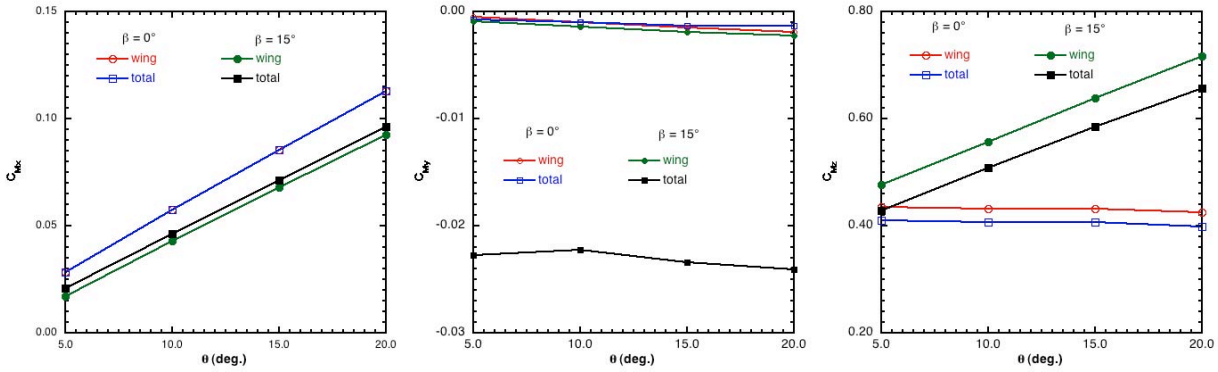

a. C_{Mx} b. C_{My} c. C_{Mz}

Fig. 14. Moment Coefficients, vehicle trim angle = 0°.

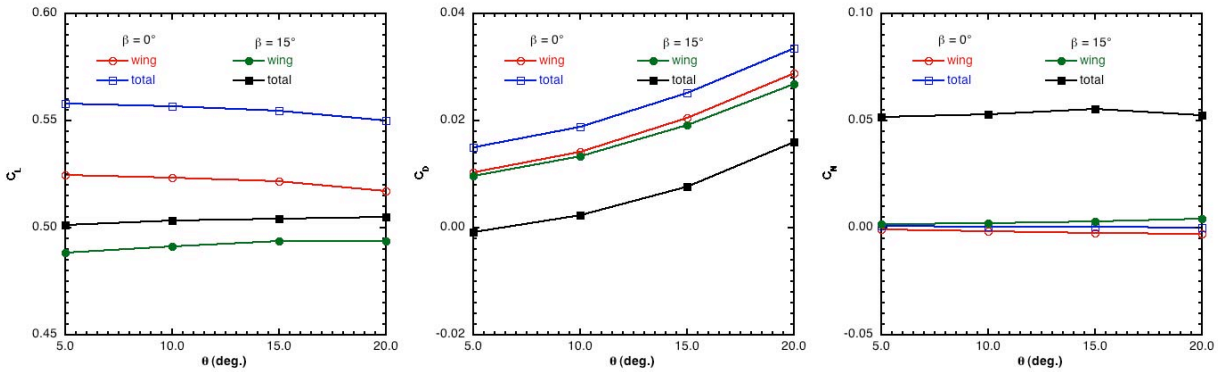

a. Lift b. Drag c. Side force

Fig. 15. Lift, drag and side force coefficients, vehicle trim angle = 3°.

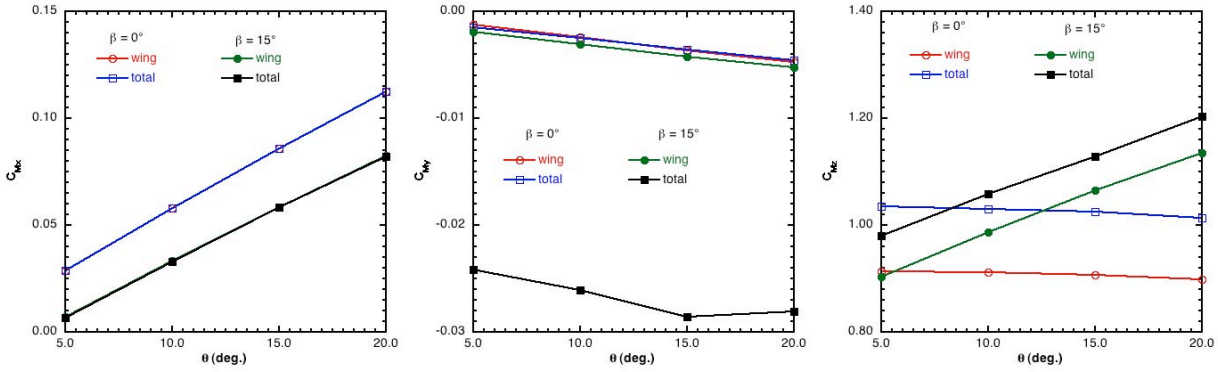

a. C_{Mx} b. C_{My} c. C_{Mz}

Fig. 16. Moment Coefficients, vehicle trim angle = 3°.

Effect of the Elevator:

The trailing 32% of the tail section is used as the elevator. This section is deflected $\delta_e = \pm 5°$, and for the side-slip angles of ±15°, for both trim conditions. The results show that C_L and C_{Mz}, Fig. 17, exhibit the maximum variation with respect to the elevator deflections, while all the other coefficients remain nearly constant.

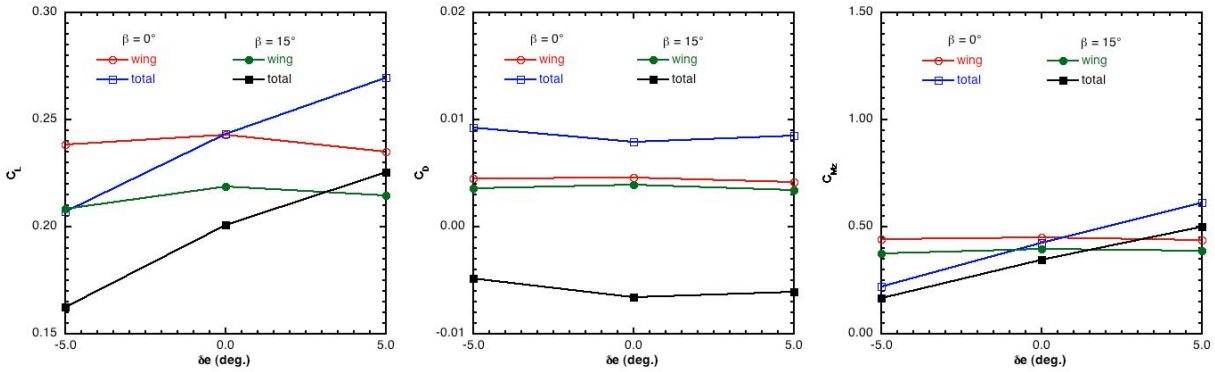

a. Lift b. Drag c. Pitch Moment

Fig. 17. Lift, drag and pitch moment coefficients, vehicle trim angle = 0°.

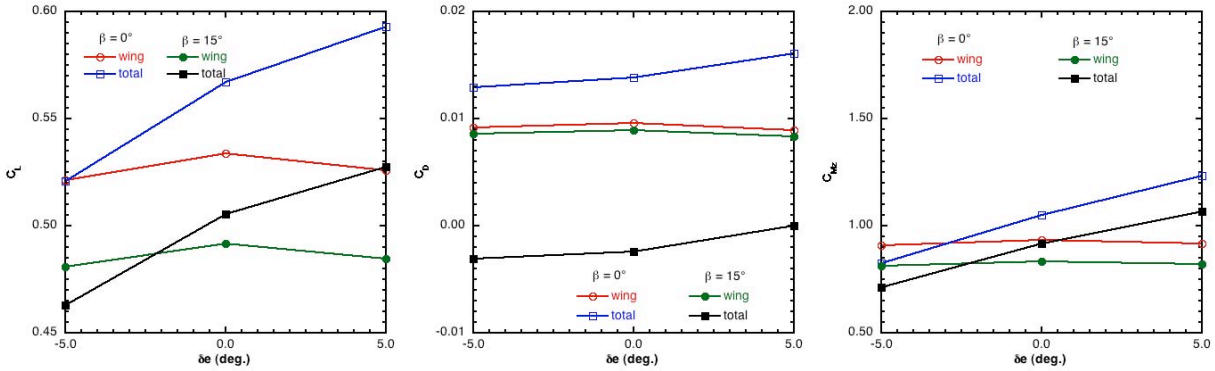

a. Lift b. Drag c. Pitch Moment

Fig. 18. Lift, drag and pitch moment coefficients, vehicle trim angle = 3°.

Deep-Stall Flow:

The vehicle configuration was modified for deep-stall flows by rotating the tail about the 1/3 chord location by 70°. The unsteady flow past this configuration was simulated at an angle of attack α = 60° and 70° and an inflow velocity V = 1.67 m/s. Figures 19a and b show the unsteady forces in the coordinate system *xyz*, Fig. 2, where *x*-axis is aligned with the inflow velocity. For α = 60°, the forces were averaged in the interval t = 4.0s and 4.5s. The mean drag force on the vehicle is 0.734 N and the mean lift force is 0.412 N. The mean pitch moment about the origin is 0.249 N-m. For α = 70°, the forces and moments were averaged in the interval t = 7.0s to 7.5s. The mean drag force is 0.85 N and the mean lift force is 0.36 N. The mean pitch moment is 0.3 N-m. Figure 20 shows the pressure distribution on the surface of the vehicle at α = 70°.

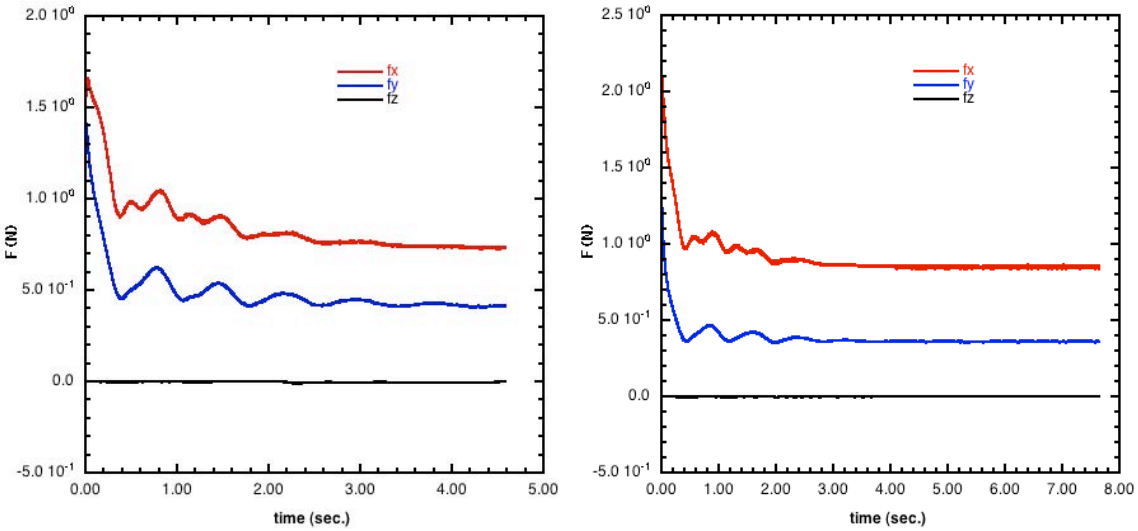

a. $\alpha = 60°$ b. $\alpha = 70°$

Fig. 19. Unsteady forces for a deep stall configuration, V = 1.67 m/s.

a. top view

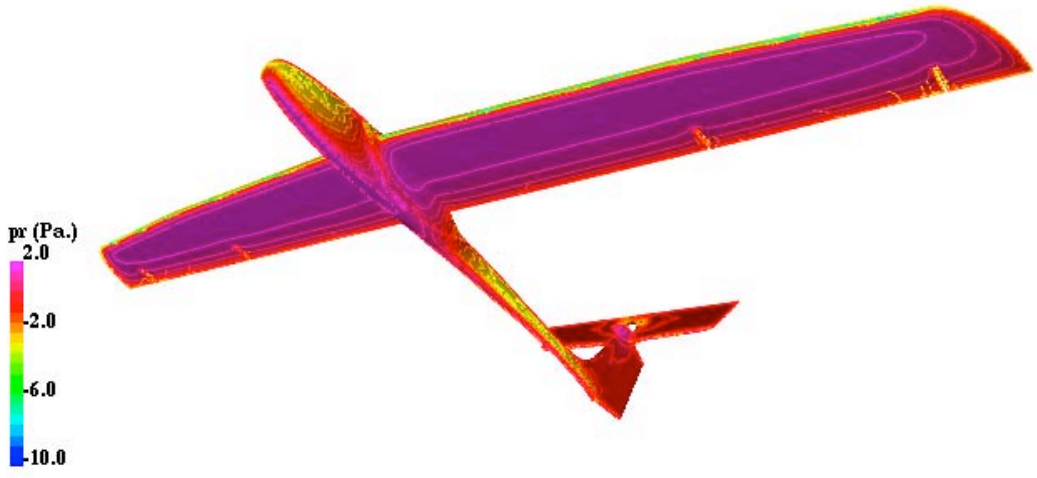

b. bottom view

Fig. 20. Surface pressure distribution on a Deep Stall vehicle, V = 1.67 m/s, $\alpha = 70°$.

The deep-stall characteristics are also obtained for a velocity V = 5.79 m/s, for a range of α's from 50° to 90°. The unsteady forces and moments were averaged over 0.5s after the initial transients have subsided and are shown in Fig. 21a and b. The drag, lift and pitch-moments are piecewise linear with two linear segments between 50° - 70° and 70° - 90°. Figure 22a and b show the variation of the mean forces and moments with side-slip angle is nearly linear for the side force an the roll and yaw moments.

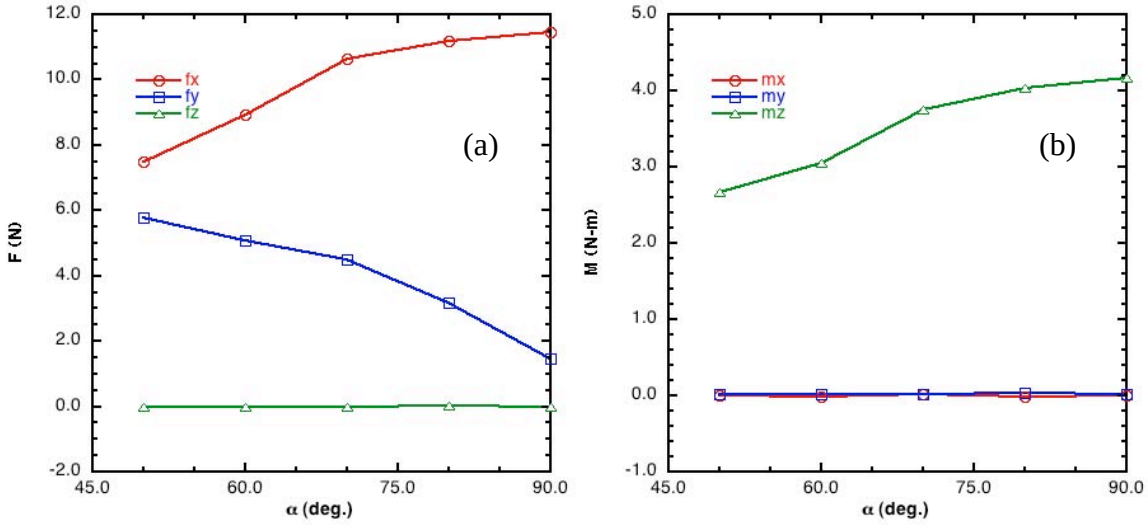

Fig. 21. Mean forces and moments for Deep-Stall vehicle, V = 5.79 m/s, β = 0°.

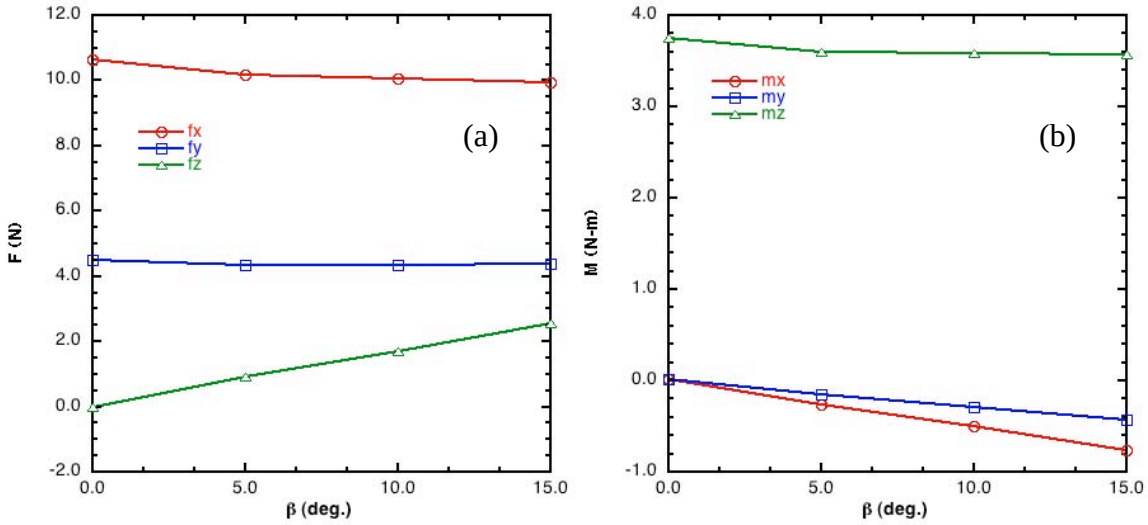

Fig. 22. Mean forces and moments for Deep-Stall vehicle, V = 5.79 m/s, α = 70°.

Next, the roll characteristics of the vehicle under deep-stall conditions were determined by deflecting the left aileron through ±20° deflections. The results show that the mean forces and moments remain nearly constant as shown in Fig. 23a and b. The effect of rudder deflection on the vehicle was studied for ±5° deflections of the rudder. The results show that the f_x = 10.4 N, f_y = 4.38 N and M_z = 3.67 N-m. The yaw moment varies from 0.027 N-m to 0.019 N-m as the rudder deflection is changed form -5° to +5°.

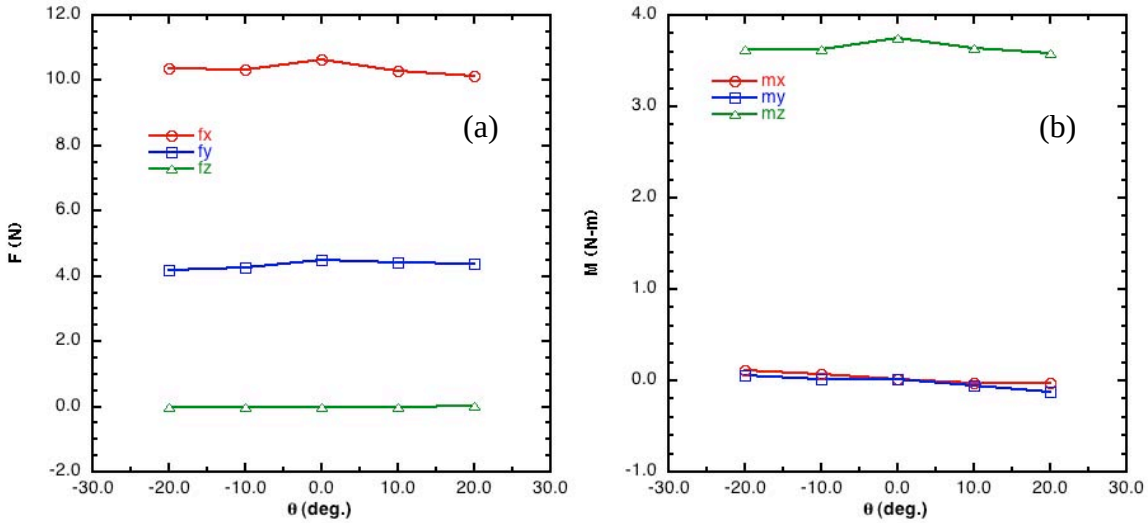

Fig. 23. Variation of Mean forces and moments for Deep-Stall vehicle with left aileron deflection, V = 5.79 m/s, α = 70°.

All of the above results were used to obtain the control derivatives used by Aaron Kahn [2] for the controller development. The unsteady trajectory of the vehicle is next computed using the vehicle properties such as mass, center of gravity and the moments of inertia about the principal axes of the vehicle. Initial simulations were performed at V = 5.79 m/s at α = 70°, with the vehicle constrained in pitch and roll. These results coupled with the controller simulations of Aaron Kahn showed that the descent rate of the vehicle would be too fast and not feasible. Hence, the configuration for the deep-stall recovery trajectory simulation was modified by setting the free stream velocity to V = 10.97 m/s at α = 40°. The tail was rotated to align with the in flow angle and both the ailerons were deflected by 15°. In addition, the vehicle was initially pitched up by 7.15°. The unsteady flow past this configuration was obtained with the trajectory of the vehicle constrained to pitch and roll due to the computed forces and moments. Also, the vehicle was constrained in all the translational degrees of freedom. The computed

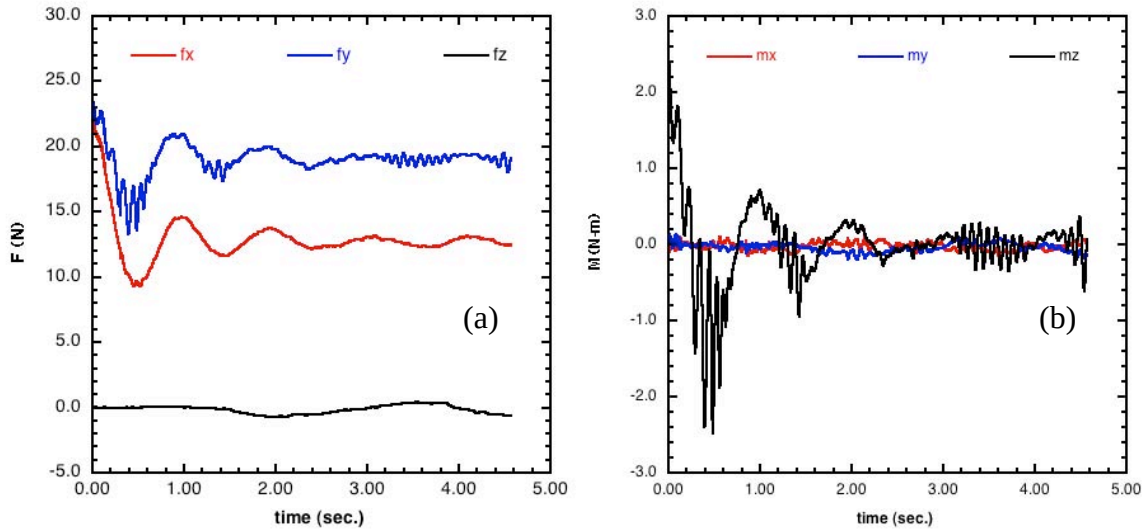

Fig. 24. Time history of forces and moments on a deep-stall vehicle, V = 10.97 m/s, α = 40°.

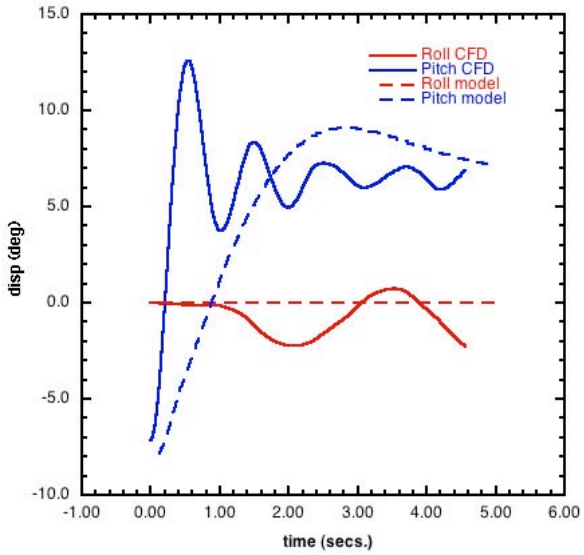

Fig. 25. Trajectory of the deep-stall vehicle, V = 10.97 m/s, α = 40°.

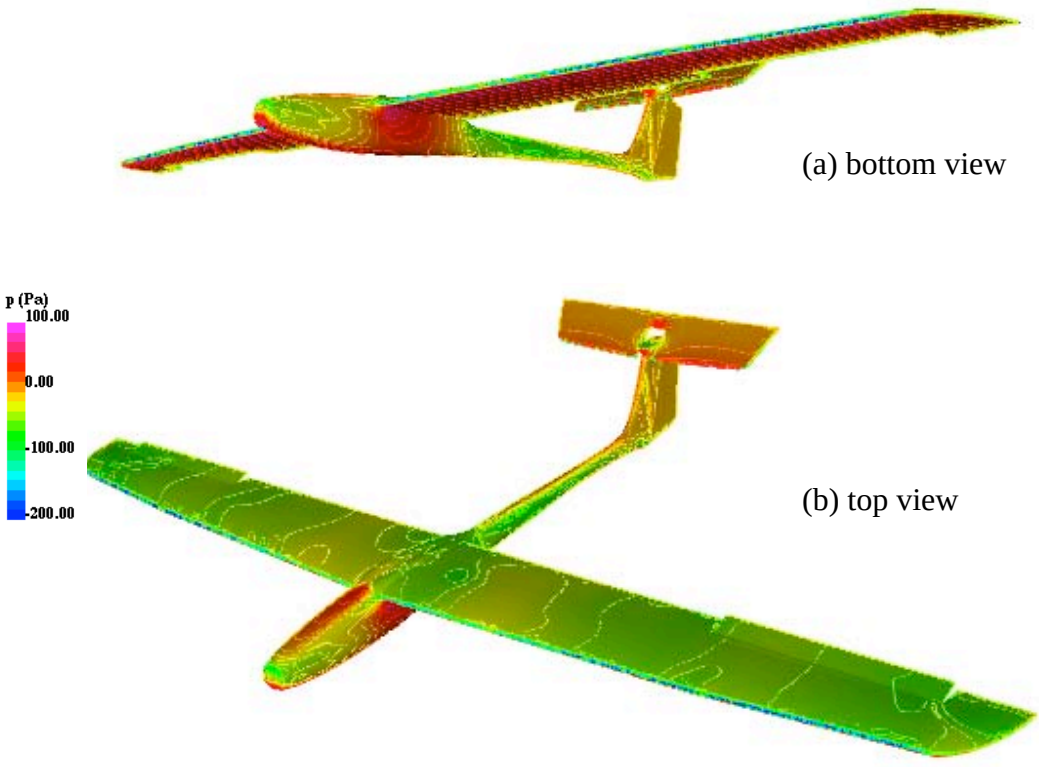

Fig. 26. Surface pressure distribution on the vehicle undergoing deep-stall maneuver, t = 2.38 s.

unsteady forces and moments are shown in Fig. 24. The pitch and roll motions of the vehicle is shown in Fig. 25. The results show that the vehicle undergoes initial pitch oscillations and settles

into a final pitch down attitude of nearly 6°, while it rolls initially and stabilizes later. The motion is consistent with the findings of the reduced model simulation of Aaron Kahn shown in Fig. 25. The instantaneous pressure distribution on the surface of the vehicle, Figs. 26a and b show the unsteadiness on the top surface of the wing and near stagnation pressure on the bottom of the wing and the fuselage. The unconstrained trajectory of the pitch and roll motions of this vehicle with differential aileron deflections were also computed. Two cases of aileron deflections were considered. The first one was with the right aileron deflected down by 15° while the left aileron is flush with the wing. For this case, the unsteady forces and moments are shown in Fig. 27 and the pitch and roll trajectory is shown in Fig. 28. The pitch motion is similar in trend to the previous case while the roll is oscillatory about positive angle of nearly 4°, as expected. The second case was simulated with the right aileron deflected up by 30° while the

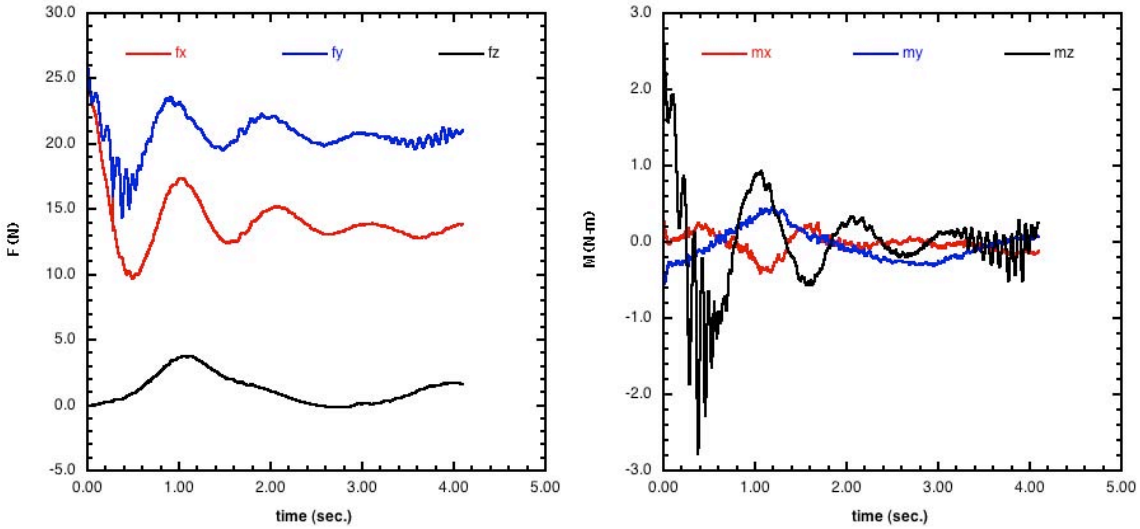

Fig. 27. Time history of forces and moments on a deep-stall vehicle with differential aileron deflection $\Delta\theta = 15°$, V = 10.97 m/s, $\alpha = 40°$.

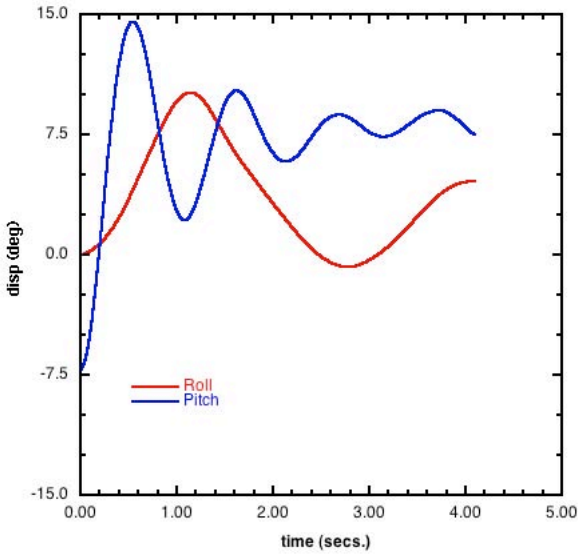

Fig. 28. Trajectory of a deep-stall vehicle with differential aileron deflection $\Delta\theta = 15°$, V = 10.97 m/s, $\alpha = 40°$.

left aileron is flush with the wing. The unsteady force and moments are shown in Fig. 29 and the trajectory of the vehicle is shown in Fig. 30. After 4s of simulation, the vehicle achieves a nearly steady downward pitch angle of 4.75° and while the roll has not achieved a quasi steady state.

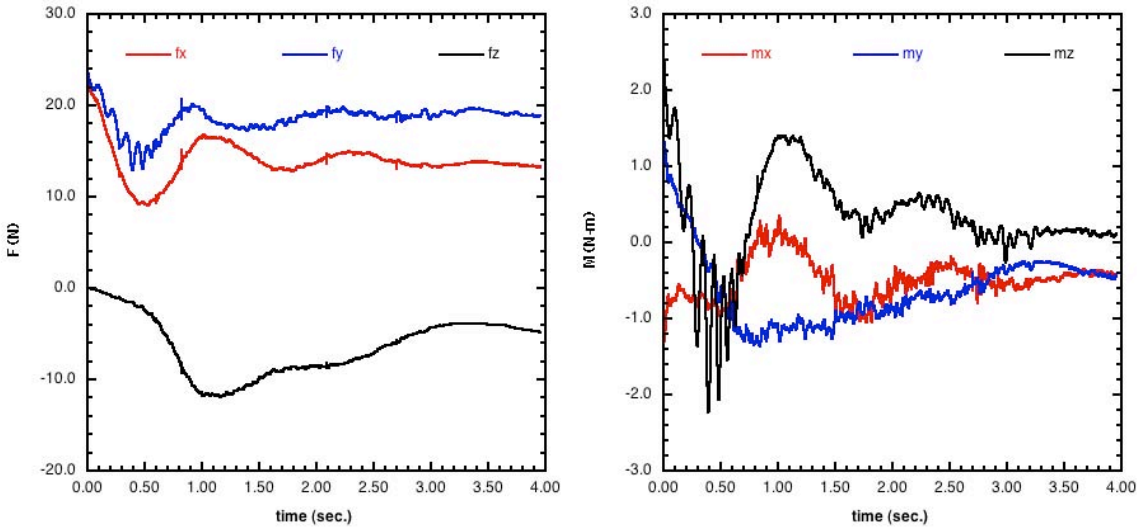

Fig. 29. Time history of forces and moments on a deep-stall vehicle with differential aileron deflection $\Delta\theta = 30°$, V = 10.97 m/s, $\alpha = 40°$.

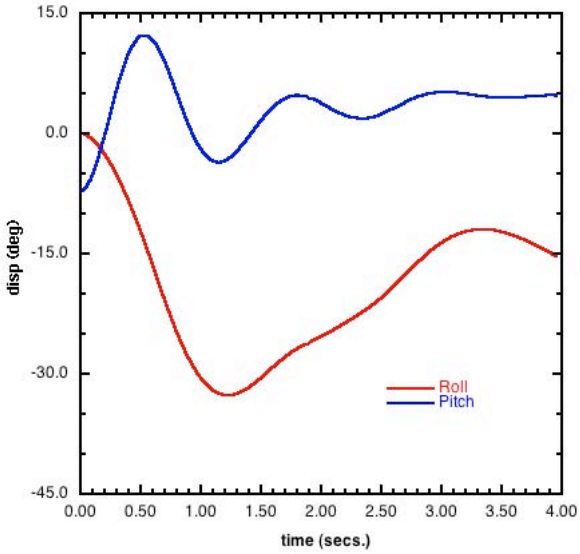

Fig. 30. Trajectory of a deep-stall vehicle with differential aileron deflection $\Delta\theta = 30°$, V = 10.97 m/s, $\alpha = 40°$.

SUMMARY

The 3-D steady and unsteady computations of the flow past a deep-stall air vehicle were performed. The aerodynamic characteristics of the vehicle were mapped out for a wide range of angles of attack, side-slip and control surface deflections. The unsteady characteristics of this vehicle were also computed in the deep-stall regime. These results were used for the development of dynamic model of the controller. For the deep-stall configurations, the unsteady forces and moments were computed by the integrating the surface distributions and the unconstrained trajectory of the vehicle is predicted based on the 6-dof model.

ACKNOWLEDGEMENTS

This work was supported by ONR through an NRL 6.2 project: "Deep Stall Fixed Wing Aircraft Guidance and Control." The valuable discussions with Mr. Aaron Kahn of TEW Division are greatly appreciated. This work was supported in part by a grant of HPC time from the DoD HPC center for the NRL SGI-Altix.

REFERENCES

1. Aerovironment, Inc. (2010). http://www.avinc.com/uas/small_uas/raven.

2. Kahn, Aaron, D., Adaptive Control for Small Fixed-Wing Unmanned Air Vehicles, *AIAA*-2010-8413, Washington, D.C., August 2010.

3. Ramamurti, R. and Löhner, R., Evaluation of an Incompressible Flow Solver Based on Simple Elements, *Advances in Finite Element Analysis in Fluid Dynamics*, FED **137**, Editors: Dhaubhadel, M. N. *et al*., ASME Publication, New York, 33-42, 1992.

4. Ramamurti, R., Sandberg, W.C. and Löhner, R., Simulation of the Dynamics of Micro Air Vehicles, *AIAA-2000-0896*, Reno, NV, January 2000.

5. Ramamurti, R. and Sandberg, W.C., A Three-Dimensional Computational Study of the Aerodynamic Mechanisms of Insect Flight**,** *J. Exp. Biol.* **205**, 1507-1518, 2002.

6. Ramamurti, R. and Sandberg, W.C., A Computational Investigation of the 3-D Unsteady Aerodynamics of *Drosophila* Hovering and Maneuvering, *J. Exp. Biol*., Vol. 210, No. 5, pp. 881-896, March 2007.

7. Rasband, W.S., ImageJ, U. S. National Institutes of Health, Bethesda, Maryland, USA, http://rsb.info.nih.gov/ij/, 1997-2009.